

Experimental Assessment and Micromechanical Modeling of Additively Manufactured Austenitic Steels under Cyclic Loading

Mahdieh Shahmardani, Ruslan Logvinov, Tomáš Babinský, Stefan Guth, Shubhadip Paul, Abhishek Biswas, Napat Vajragupta, and Alexander Hartmaier*

The present work deals with the cyclic deformation behavior of additively manufactured austenitic stainless steel 316L. Since fatigue experiments are complex and time-consuming, it is important to develop accurate numerical models to predict cyclic plastic deformation and extrapolate the limited experimental results into a wider range of conditions, considering also the microstructures obtained by additive manufacturing. Herein, specimens of 316L steel are produced by powder bed fusion of metals with laser beams (PBF-LB/M) with different parameters, and cyclic strain tests are performed to assess their deformation behavior under cyclic loads at room temperature. Additionally, a micromechanical model is set up, based on representative volume elements (RVE) mimicking the microstructure of the experimentally tested material that is characterized by electron backscatter diffraction (EBSD) analysis. With the help of these RVEs, the deformation-dependent internal stresses within the microstructure can be simulated in a realistic manner. The additively manufactured specimens are produced with their loading axis either parallel or perpendicular to the building direction, and the resulting anisotropic behavior under cyclic straining is investigated. Results highlight significant effects of specimen orientation and crystallographic texture and only a minor influence of grain shape on cyclic behavior.

components with complex geometry.^[1] Specifically for the powder bed fusion (PBF) process, a metallic powder is first spread on the build platform using diverse coater mechanisms, and an energy source melts it according to the input provided by the computer-aided design model of the part to be produced. The process continues with successive spreading and melting of powder layers until the desired component is manufactured. PBF processes include melting with laser beams and electron beams.^[2] Repeated reheating and re-cooling processes of the previous molten and solidified layers lead to a complex thermal process drastically affecting the microstructure of AM components, typically ranging from large columnar to small equiaxed grains.^[3]

A vast majority of premature failures of mechanical components occurs due to fatigue. Even though high cycle fatigue is mostly the limit state due to relatively small imposed stresses below the yield limit of the material, low cycle fatigue and related mechanisms come into question once the


yield limit is exceeded, which might occur due to start-up and shut-down operations in thermal engines, for example, in energy conversion. Since low-cycle-fatigue experiments are complex and expensive, many studies have focused on modeling the fatigue

1. Introduction

Additive manufacturing (AM) of metallic components has emerged as a promising technique for manufacturing large

M. Shahmardani, S. Paul, A. Biswas, N. Vajragupta, A. Hartmaier
Interdisciplinary Centre for Advanced Materials Simulation (ICAMS)
Ruhr-Universität Bochum
Universitätsstr. 150, 44801 Bochum, Germany
E-mail: alexander.hartmaier@rub.de

R. Logvinov
Siemens AG
T AMM COA-DE
Siemensdamm 50, 13629 Berlin, Germany

 The ORCID identification number(s) for the author(s) of this article can be found under <https://doi.org/10.1002/adem.202300103>.

© 2023 The Authors. Advanced Engineering Materials published by Wiley-VCH GmbH. This is an open access article under the terms of the Creative Commons Attribution License, which permits use, distribution and reproduction in any medium, provided the original work is properly cited.

DOI: 10.1002/adem.202300103

T. Babinský
Institute of Physics of Materials
Czech Academy of Sciences
Žitkova 22, 61600 Brno, Czech Republic

S. Guth
Institute for Applied Materials
Karlsruhe Institute of Technology (KIT)
Engelbert-Arnold-Straße 4, 76131 Karlsruhe, Germany

S. Paul
Department of Metallurgical and Materials Engineering
National Institute of Technology Durgapur
Durgapur, West Bengal 713209, India

A. Biswas, N. Vajragupta
Integrated Computational Materials Engineering
VTT Technical Research Centre of Finland Ltd.
02044 Espoo, Finland

behavior and on attempting to determine the properties to describe the fatigue behavior.^[4–6] To investigate the influence of microstructural texture, loading direction, temperature, and other factors, precise numerical modeling is necessary. This becomes even more important in the case of AM materials with their unique microstructure having arisen due to the complex thermal history. Hence, a powerful computational tool is needed to predict the mechanical behavior of metals produced by AM techniques with complex microstructures. Micromechanical modeling has proven to be a suitable computational approach for predicting the macroscopic mechanical behavior, taking into account the material microstructure properties.^[7–10] To accurately describe the mechanical behavior of AM materials by numerical simulations, synthetic representative volume elements (RVEs) were generated in a way that they are statistically equivalent to the experimentally observed microstructure and are also computationally efficient.^[11]

Furthermore, micromechanical modeling can improve our understanding of the microstructure–property relationships of crystalline materials,^[12,13] which is the basis for a systematic improvement in fatigue properties. In one study, the interactions between the microstructure and the dissipative deformation mechanisms of steel were exploited to optimize the microstructure.^[14] The authors proposed a micromechanical model to find the relation between microstructure properties and dissipative mechanisms related to deformation. Results showed that dissipation is insensitive to grain size but mostly affected by grain size distribution and grain orientation. In another study, the mechanical behavior of transformation induced plasticity (TRIP) steel under cyclic loading was investigated and it was found that the martensite phase affects the cyclic deformation behavior.^[15] The authors proposed a constitutive model including kinematic hardening, which could predict the cyclic behavior taking into account the phase transformation occurring in the microstructure of the TRIP steel. The influence of dual-phase (DP) steel under cyclic loading was studied numerically and validated by experimental data.^[16] A micromechanical model was developed considering microstructure features and a dislocation density-based hardening model for each phase. This model was used to describe the low-cycle-fatigue behavior of DP steel. Results were found in good agreement with experimental data in terms of stress–strain hysteresis loops.

Even for more complex loading situations, studies showed that micromechanical modeling can successfully assess the influence of multiaxial nonproportional loading paths.^[17–19] The effect of different loading paths on mean stress and fatigue lives was evaluated by micromechanical studies on polycrystalline materials under low-cycle-fatigue loading.^[20] These authors developed an RVE model, considering the orientation of each grain, and proposed an inelastic damage model to simulate polycrystalline material behavior. The model predicted fatigue lives and the occurrence of microheterogeneities in the RVE due to damage under different cyclic loading directions. The influence of a non-proportional loading history on 316L steel under cyclic loading was studied numerically in ref. [21] where the authors proposed a viscoplastic constitutive model, including the Ohno–Wang kinematic relation and a Marquis isotropic hardening rule. The numerical model could predict the hardening behavior under

cyclic loading in good agreement with experimental results, but it was less successful in simulating the softening effect.

It is the aim of the present study to investigate the influence of material texture, grain morphology, and loading direction on the low-cycle-fatigue behavior of 316L steel manufactured by powder bed fusion of metals with laser beams (PBF-LB/M) and to implement and parameterize a suited crystal plasticity model that results in a satisfying agreement between the micromechanical modeling and the experimental data for all given microstructural states. To accomplish this, 316L specimens were additively manufactured by PBF-LB/M with different orientations of the loading axis to the building plane. The mechanical properties of these specimens are assessed in strain-controlled fatigue experiments and the microstructure and crystallographic texture is characterized by means of electron backscatter diffraction (EBSD). In a further step, a micromechanical model including a representation of the true microstructure and a crystal plasticity-based constitutive law are implemented and applied to simulate the material behavior under cyclic loading with material parameters determined in an inverse procedure in previous work.^[22]

2. Material Preparation, Testing, and Microstructure Analysis

The specimens of 316L steel were produced by PBF-LB/M with standard parameters from SLM-Solutions for layer thicknesses

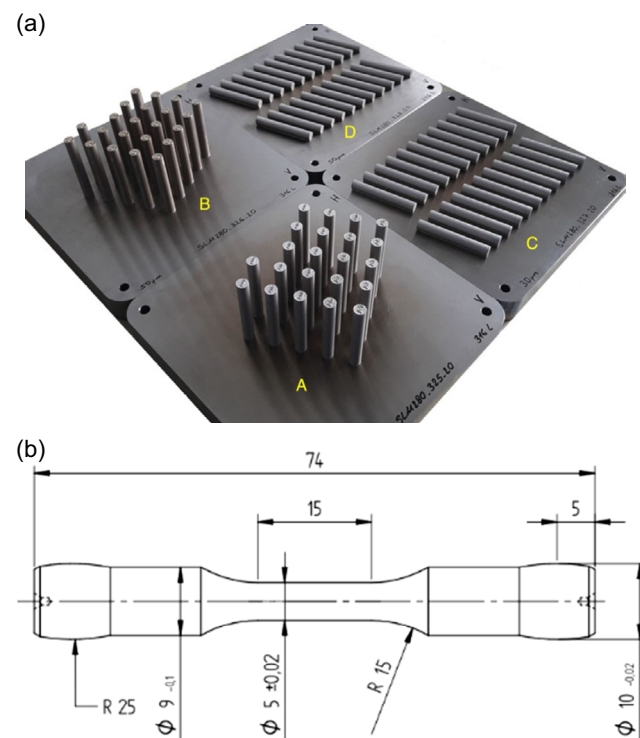


Figure 1. a) Additively manufactured specimens on their building plates. Specimen types A and B were manufactured with the loading axis along the building direction, whereas for specimen types C and D the loading axis lies in the building plane. b) Technical drawing of test specimen geometry manufactured from the cylindrical shapes.

of 30 μm (A- und C-type) and 50 μm (B- und D-type) on an SLM280HL device. As shown in **Figure 1**, types A and B were produced with the loading axis along the building direction, whereas for types C and D, the loading axis is lying in the building plane. After the manufacturing process, the specimens were heat treated for 2 h at 600 °C on the building plate to relieve the stresses and, finally, all specimens were separated from the building plate.

For the cyclic strain tests, solid round specimens with a gauge length of 10 mm and a gauge length diameter of 5 mm were machined from the additively manufactured raw bars. The tests were performed on a computer-controlled servo-electric Zwick testing machine with a 50 kN load cell. The strain was measured using a capacitive extensometer with 10 mm gauge length, which was attached to the specimens by alumina rods. For all tests, the strain course had a sawtooth shape going 60 s into compression and 30 s into tension, that is, the initial loading was compressive. A strain amplitude of 0.5% was applied during testing, and the tests were stopped after 5000 cycles. For all tested specimens the loading did not produce a macroscopic crack; hence, the fatigue lifetime was not determined. The cyclic straining was uniaxial and fully reversed ($R_e = -1$). All tests were conducted at room temperature in laboratory air.

A microstructural analysis of the material was performed with scanning electron microscopy with an electron back scatter detector yielding the grain morphology and the crystallographic texture. To accomplish this, the samples for microscopic analysis have been cut from the shoulders of the tested specimens, that is, from regions that have neither been exposed to thermal nor to mechanical loads. After cutting, the samples have first been mechanically polished and subsequently electropolished. The EBSD analysis was performed with a scanning electron microscope (SEM) of type FEI Quanta FEG 650 equipped with an EBSD detector of type EDAX Ametek Hikari. Data were collected with an acceleration voltage of 20 kV and a step size of 0.5 μm . Since the grain shapes are significantly elongated, for each specimen two directions were analyzed: 1) the top view of the specimen, that is, the plane normal to the testing direction, and 2) the side view of the specimen, transversal to the testing direction. Note that for specimen types A and B, the loading axis matches the build direction, whereas these axes are normal to each other for types C and D. The statistical information about grain size, grain shape, and orientation of the major axis was obtained for the microstructure of each specimen, forming the basis for the generation of micromechanical models, as described in the next section.

As seen in the EBSD micrographs shown in **Figure 2–5**, the microstructure of all batches exhibits a strong directionality, where the grains are significantly elongated with typical aspect ratios around 2:1 but reaching values of 5:1 and higher for some grains. The major axis of the grains is roughly oriented into the building direction; however, the standard deviation of the orientation angle is rather large and amounts to 35° or more in some cases. When viewed along the building direction, the grains exhibit a rather equiaxed shape, but some of them appear to be half-moon shaped or even annular, which is explained by shadowing effects of smaller grains lying on top of larger ones, as seen from the view transversal to the building direction. Furthermore, in both views, the scanning direction of the laser beam during the additive manufacturing process produces visible traces in the microstructure.

Another common feature of all tested batches, except for the specimen of type D, is a significant $\langle 110 \rangle$ texture along the building direction. For samples A, B, C, the texture index lies around 2.7, whereas for sample D it is only 2.0. The texture of the EBSD maps was analyzed with the MTEX toolbox available for commercial software MATLAB.^[23] For the automated detection of grain boundaries, the threshold value for the misorientation was set to 5°. Furthermore, features with less than 4 pixels have not been taken into account, to compensate the influence of noise and individual pixels that are not properly indexed.

In **Figure 2**, the microstructure of a specimen of type A is shown in form of EBSD maps. The analysis module of the MTEX toolbox has been applied to assign an ellipsis to each identified grain from which the equivalent diameter, aspect ratio, and orientation of the major axis are obtained; see Appendix A, Supporting Information, for an example of this analysis. Furthermore, the grain orientations are quantified via pole figures of the orientation distribution function (ODF) of the measured grain orientations. The microstructure is analyzed as viewed along the building direction, corresponding to the loading direction for specimens of type A and B, and also along the transverse direction. In the latter view, the elongation of the grains is well visible. A common feature of both views is that the grains appear to be staggered on top of each other, which produces very small features in the EBSD map. Hence, the analysis of the equivalent diameter of the grains, defined as the diameter of the circle, which has the same area as the ellipses assigned to each grain in the EBSD map, produces a rather broad log-normal distribution with a shape parameter of 7.9 μm , which can be considered as the average feature size and consequently a characteristic length scale of the microstructure. This length scale is important for the generation of a numerical microstructure model and will be further analyzed in the next section.

In **Figure 3**, a specimen of type B is characterized, which is also standing on the building plate, that is, the building direction corresponds to the loading axis. Compared with specimens of type A, the layer thickness has been increased from 30 to 50 μm during the additive manufacturing process. A visual inspection of the micrographs, in particular those of the side views, reveals that the microstructure is somewhat more regular. However, there is still a lot of small features present, and the length scale found in the distribution of equivalent diameters of all grain amounts to 13.3 μm . Thus, it can be said that the increase in the layer thickness of a factor 1.67 in the additive manufacturing of batches of type A and B is mirrored in the length scales of the resulting microstructures, which differs by a factor of 1.65.

In **Figure 4**, the microstructure of a specimen of type C is characterized, which is lying in the building plane of the PBF process, such that the loading axis in the mechanical tests is normal to the building direction. Consequently, the microstructure characteristics between type C specimens are exchanged with those of type A and B specimens. The layer thickness during the manufacturing of these specimens was 30 μm , and the resulting microstructural length scale is 7.1 μm , matching that of specimen type A, which has been built with the same layer thickness. Also, the $\langle 110 \rangle$ texture in the crystallographic orientation of grains is comparable between these specimen types.

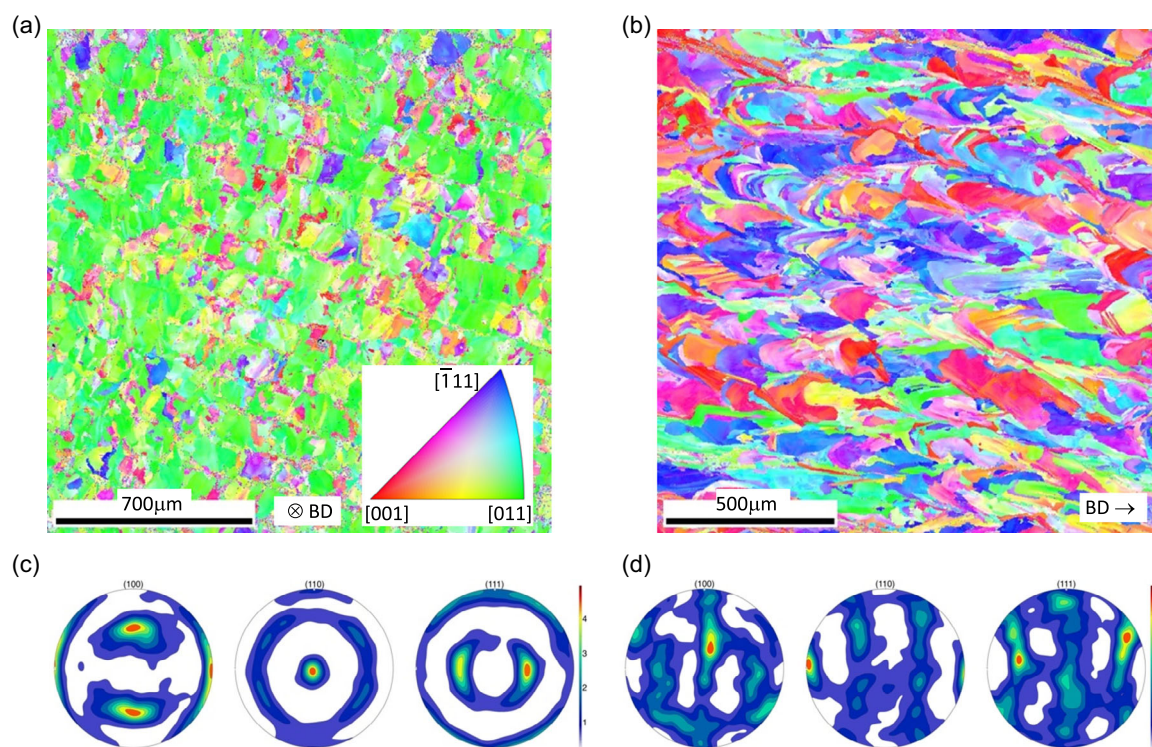


Figure 2. Microstructure details of specimen A, EBSD map from a) top view, that is, along loading axis and building direction (BD), b) side view; corresponding ODF pole figures from c) top view and d) side view of specimen. In this work, the inverse pole figure key given in subfigure (a) is the same for all EBSD maps presented, and for all ODF plotted, the individual pole figures represent the [100], [110], and [111] axis from left to right.

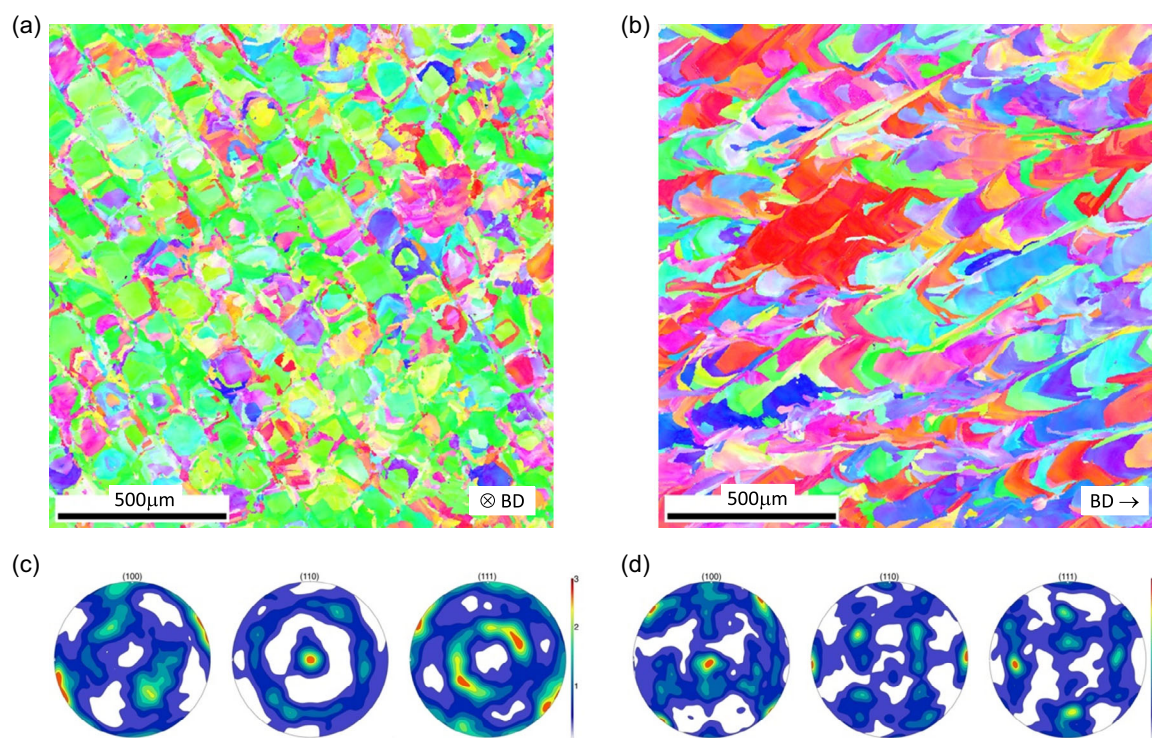


Figure 3. Microstructure details of specimen B, EBSD map from a) top view and b) side view, corresponding ODF pole figures from c) top view and d) side view of specimen. Figure annotations are the same as in Figure 2.

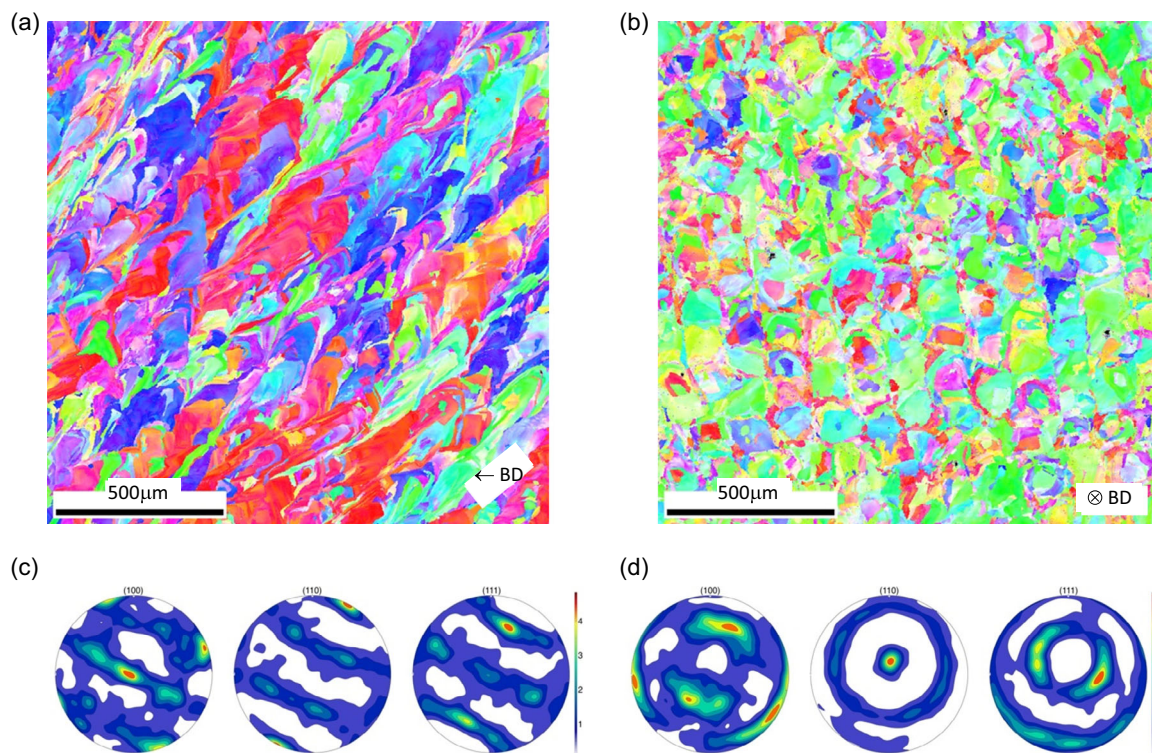


Figure 4. Microstructure details of specimen C, EBSD map from a) top view and b) side view, corresponding ODF pole figures from c) top view and d) side view of specimen. Figure annotations are the same as in Figure 2.

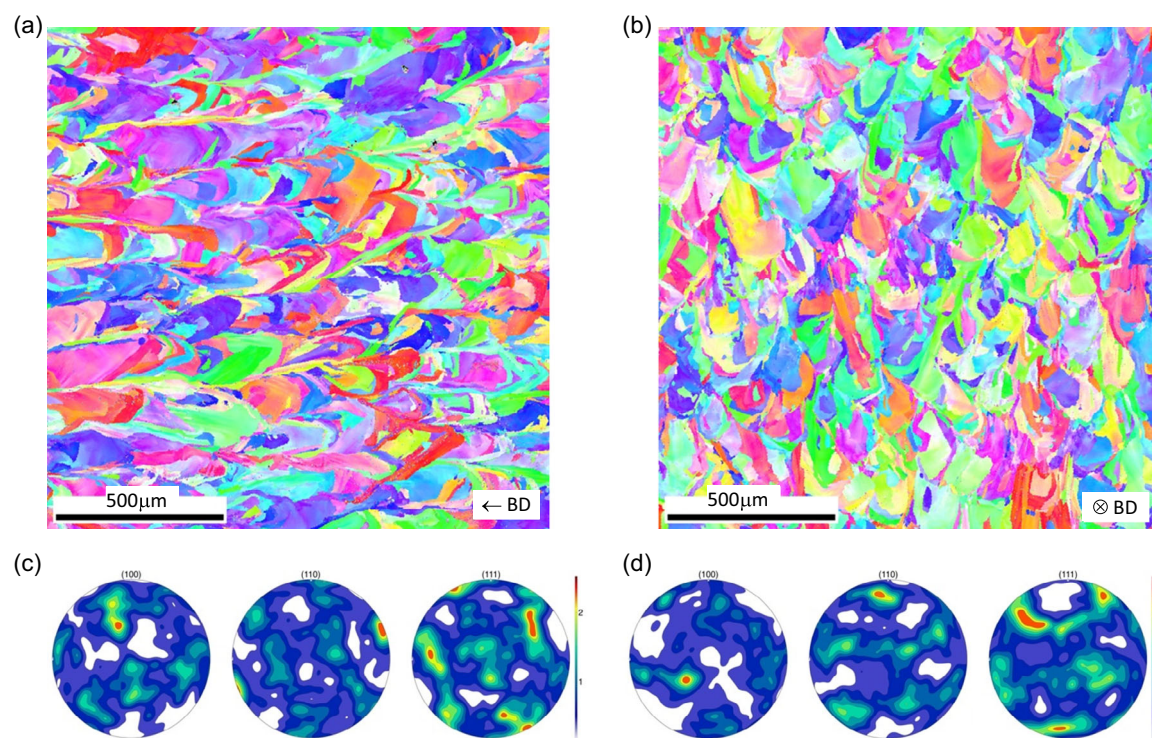


Figure 5. Microstructure detail of specimen D, EBSD map from a) top view and b) side view, corresponding ODF pole figures from c) top view and d) side view of specimen. Figure annotations are the same as in Figure 2.

The microstructure of the specimen of type D, as visualized in Figure 5, reveals qualitatively the same trends as the other specimens; however, its texture is somewhat less pronounced. The microstructural length scale amounts to $9.3\ \mu\text{m}$, being somewhat smaller than that of specimen B, produced with the same layer thickness, but still significantly larger than in specimens A and C, produced with a smaller layer thickness. It is noted that the identification of the building direction from the tested specimen characterized here bears some uncertainty. As the tested specimen (D1) has been extracted from the edge of the building plate, another untested sample from the center of the building plate (D15) has been analyzed microscopically. As shown in the results, shown in Appendix B, Supporting Information, the texture of this sample D15 is consistent to that of specimen types A, B, and C presented above. Hence, the deviation of the texture of the tested specimen is attributed to its position close to the edge of the building plate.

3. Numerical Modeling

To obtain the numerical response of the austenitic steel under cyclic loading, micromechanical models were developed, taking into account microstructure properties obtained from EBSD

analysis. The generation of RVE was performed with the open source software toolbox Kanapy,^[24] developed at ICAMS^[25]; in this process, the morphology of the experimental microstructure was represented in a statistical sense and also the crystallographic orientations of the grains were chosen to match the experimental texture, including the misorientation between the grains.^[26] Based on these RVEs, finite-element models were generated for the commercial software Abaqus, as described in the following sections.

3.1. RVE Generation and Finite-Element Modeling

The geometries of the generated RVEs based on the four specimens' microstructural details described in Section 2 are visualized in Figure 6, where the grain shapes for all specimen types are seen. The 3D microstructures are represented by a regular mesh of $30 \times 30 \times 30$ voxels assigned to individual grains. The side length of each voxel is set to $1\ \mu\text{m}$. It is visible in the RVEs that the grain size for batches B and D is larger than for batches A and C. The developed RVEs consist of 88–100 grains, taking into account the statistical microstructural features, as equivalent grain diameter, aspect ratio, and orientation distribution of the major grain axis, which are collected on the basis of the EBSD analysis, see Figure 7. This relatively small number of

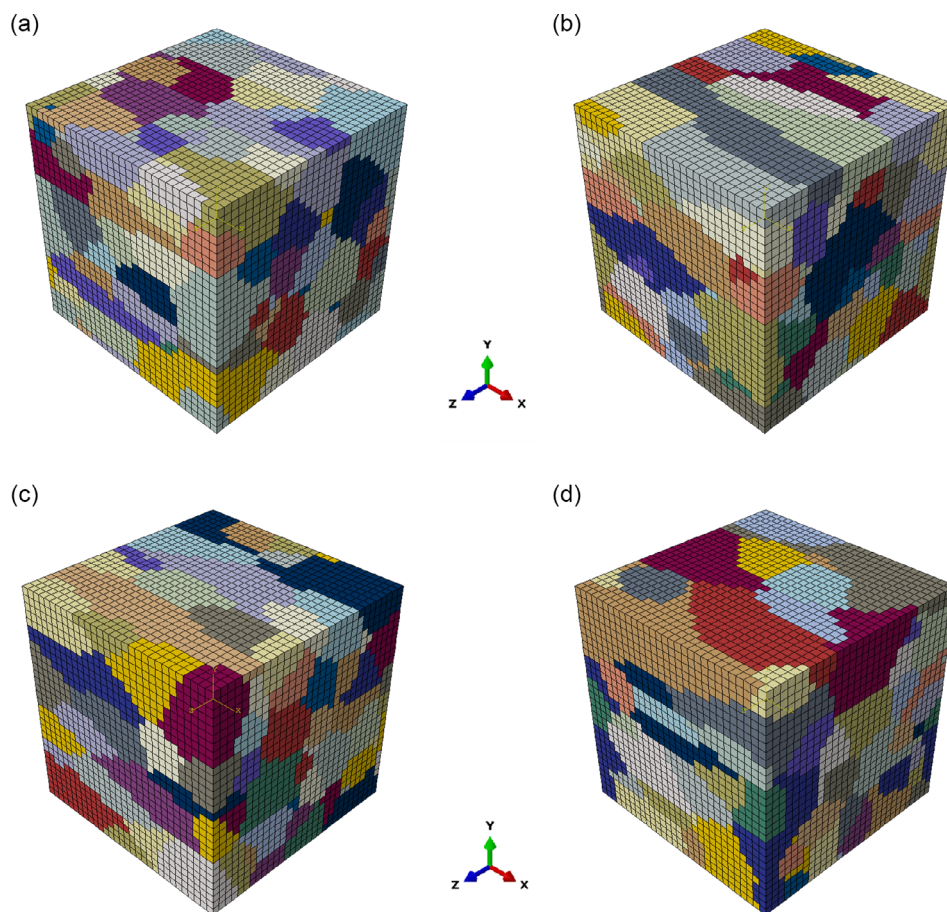


Figure 6. RVE generated for a) sample A with 96 grains, b) sample B (88 grains), c) sample C (100 grains), and d) sample D (95 grains) based on the EBSD analysis of additively manufactured specimens.

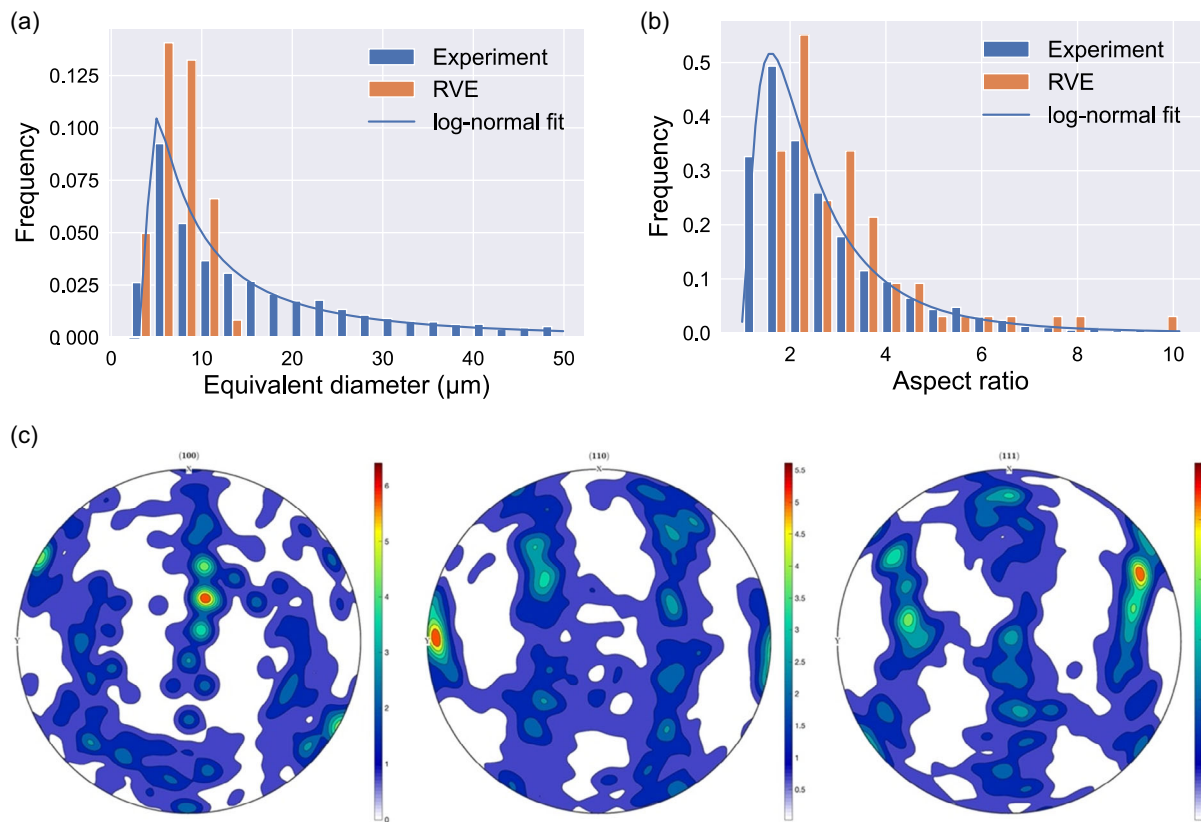


Figure 7. Microstructure properties of batch A used for the generation of its RVE based on the EBSD analysis, histograms of a) equivalent diameters of grains, b) aspect ratios of grains, and c) ODF of the 96 grain orientations represented in the RVE.

grains still represents the crystallographic texture and the resulting macroscopic properties in a good way, by virtue of an optimized generation of grain orientations, as discussed in ref. [26]. Later on, it will be seen that there is a significant difference in the mechanical response between RVEs with a random texture and the realistic texture found in experiment. All RVEs were generated such that the grain structures are periodic with respect to the simulation box. This is necessary, because the loads during the mechanical simulations were applied in form of periodic boundary conditions. Please note that the building direction for all RVEs corresponds to the x -axis such that the experimental loading axis for specimens of type A and B also is the x -axis, whereas for types C and D it is the z -axis.

In Figure 7a, the statistical distribution of equivalent diameters of the 3D grains in the RVE is compared with that of the grains identified on the EBSD map of sample A. It is seen that the distribution of equivalent diameters obtained from experiment follows a log-normal distribution, which had been used to quantify a length scale parameter for the different microstructures before. It is noted here that it is prohibitive to reconstruct the full range of equivalent diameters found in experiment within the RVE because the resolution or voxel size is determined by the smallest features that need to be represented, whereas the size of the RVE, or the total number of voxels, is determined by the largest features that are to be included. In this work, we decided to reproduce the most frequent microstructural

features in a representative way, but to cut off large features in order to keep the total size of the models in a range where it still can be handled efficiently within a finite element model, which corresponds to a cube of side length $30\ \mu\text{m}$ for all RVEs covered here. This choice of the model dimensions is based on previous work, where the different factors influencing the macroscopic mechanical response of the model have been analyzed in detail.^[27] Since we applied a local crystal plasticity model in the finite-element simulations, the length scale itself has no influence, but the arrangement and the neighborhoods of grains influence the macroscopic behavior of the model.

In Figure 7b, the statistical analysis of the grain aspect ratios is presented, again in comparison to the experimental values determined from the EBSD map of sample A and the values of the grains represented in the 3D RVE. It can be seen that the distribution of the aspect ratios follows a log-normal distribution, which is approximated by the grains in the RVE.

Finally, Figure 7c provides the ODF pole figure of the crystallographic orientations of the 96 grains in the RVE. It matches the experimental ODF obtained for a much larger number of grains with a very good accuracy, see Figure 2d. This accurate description of the texture by a reduced set of grain orientations is achieved by applying the method described in ref. [26]. This method not only reproduces the ODF with a high accuracy but also considers the misorientation distribution of neighboring grains in a realistic way. Hence, it can be said that the RVE of

batch A matches the experimental microstructure in a statistical sense. The detailed statistical analyses for batches B, C, and D are rather similar and given in Appendix C, Supporting Information, for completeness.

A finite-element model was implemented with 8-node brick elements (C3D8) matching the voxels of the RVE and consisted of 27 000 elements. Periodic boundary conditions were applied to four reference nodes as visualized in **Figure 8** to assess the macroscopic mechanical response of the generated RVEs. The important feature of periodic boundary conditions is that the degrees of freedom of nodes from one side of the model are coupled to their counterparts on the opposite side. Hence, the deformation states in the numerical model were applied to the reference nodes, and the other boundary nodes followed their kinetics.

Symmetric cyclic tensile–compressive displacement boundary conditions with $R = -1$ were applied to load the finite element model under strain-controlled conditions with an amplitude of 0.5%. The loading kinetics of the finite-element model matched those of the experimental tests.

3.2. Crystal Plasticity Model

In the finite-element model, the material behavior was implemented as a user-defined material (UMAT) subroutine in ABAQUS 2016.^[28] The elastic behavior was described by anisotropic elastic constants and a phenomenological local crystal plasticity model was used to determine the plastic cyclic response of the austenitic steel. It is worth noting that the grain size in specimens B and D was larger than in specimens A and C but their mechanical responses under cyclic loading from the performed experimental tests were very similar. As seen in **Figure 9**, there was no significant difference in the cyclic response of the pairs A and B (with different grains sizes but their loading axis parallel to the building direction) and C and D (loading axis normal to building direction). Since, in contrast, the influence of the orientation of loading axis with respect to the building direction is seen to have a significant influence on the mechanical response, the effect of the grain size was neglected in the present analysis and a local crystal plasticity model was used such that the focus of this investigation lies on the analysis of the relation between texture and mechanical behavior.

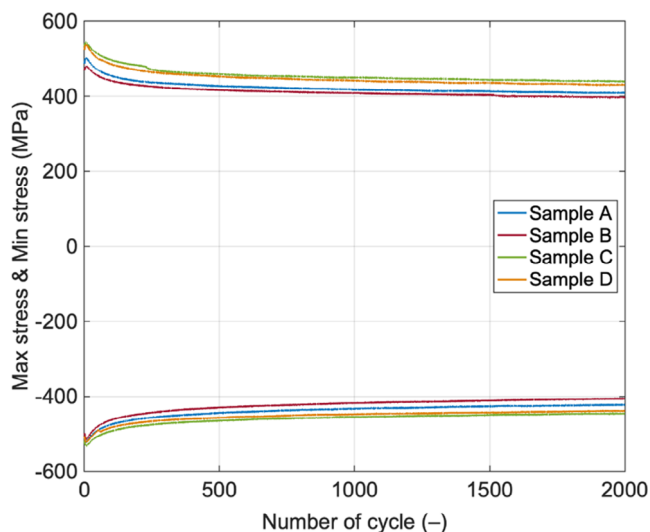


Figure 9. Experimental cyclic hardening/softening curves of PBF-LB/M 316L steel, cycled at room temperature at a total strain amplitude $\epsilon_a = 0.5\%$ in the representation of maximum and minimum stress versus number of cycles.

The used crystal plasticity model has been described in more detail in ref. [8] and is only briefly summarized here. With the assumption of finite strain deformation and based on the multiplicative decomposition of the deformation gradient F into elastic F^e and plastic F^p components, as

$$F = F^e F^p \quad (1)$$

in the intermediate configuration, it was assumed that for austenitic steel with face-centered-cubic (FCC) crystal structure, plastic deformation occurs only due to dislocation slip on the $12 \langle 110 \rangle \{111\}$ crystallographic slip systems. Hence, the plastic velocity gradient L^p was obtained by the superposition of crystallographic slips on the different slip systems α via

$$L^p = \dot{F}^p F^{p-1} = \sum_{\alpha=1}^{N_{\text{slip}}} \dot{\gamma}^{\alpha} \mathbf{d}^{\alpha} \otimes \mathbf{n}^{\alpha} \quad (2)$$

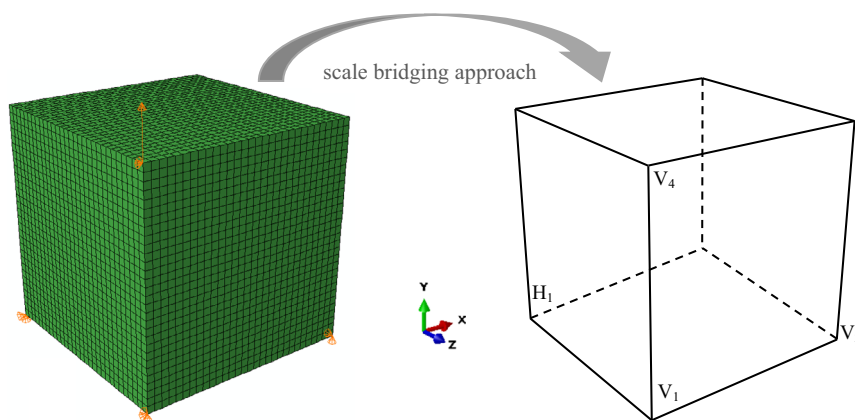


Figure 8. Finite-element model together with applied periodic boundary conditions.

where \mathbf{d}^α and \mathbf{n}^α represent the unit vectors in slip direction and normal to the slip plane in intermediate configuration, respectively. The dyadic product (\otimes) defines the Schmid tensor for slip system α . The elastic finite strain measure E^e was derived using the definition of the Green–Lagrange strain tensor

$$E^e = \frac{1}{2} (F^{eT} F^e - I) \quad (3)$$

Then, in the intermediate configuration, the second Piola–Kirchhoff stress \tilde{S} was calculated based on the elastic finite strain and stiffness tensor as

$$\tilde{S} = \mathbb{C} : E^e \quad (4)$$

where \mathbb{C} represents the fourth-order elasticity tensor. With the assumption of only small elastic strain for the metallic materials, the resolved shear stress on each slip system was approximately obtained by

$$\tau^\alpha \approx \tilde{S} : (\mathbf{d}^\alpha \otimes \mathbf{n}^\alpha). \quad (5)$$

Hence, the flow rule during plastic deformation was governed by

$$\dot{\gamma}^\alpha = \dot{\gamma}_0 \exp\left(-\frac{Q}{RT}\right) \left| \frac{\tau^\alpha - \chi_b^\alpha}{\tau_{c,0}^\alpha} \right|^{p_1} \text{sign}(\tau^\alpha - \chi_b^\alpha) \quad (6)$$

where the Arrhenius term with the activation energy Q , gas constant R , and temperature T considers thermal effects in the flow rule. It is worth noting that all numerical analyses in this study were done at room temperature although the model was parameterized for a rather wide temperature range. The prefactor $\dot{\gamma}_0$ represents a reference shear rate; χ_b^α and $\tau_{c,0}^\alpha$ are resolved back stress and the critical resolved shear stress of each slip system α . The evolution of the back stress, which describes the kinematic hardening behavior of the material under cyclic loading, was calculated based on the proposed Ohno–Wang relation^[29] as

$$\dot{\chi}_b^\alpha = A \dot{\gamma}^\alpha - B \left(\frac{|\chi_b^\alpha|}{A} \right)^M \chi_b^\alpha |\dot{\gamma}^\alpha| \quad (7)$$

where A and B are fitting parameters, and the exponent M controls the dynamic recovery term under cyclic loading. The functionality of M is activated once the ratio A/B reaches a saturation level.

The experimental cyclic tests of 316L reveal a rather small amount of cyclic softening in their stress amplitude with respect to the number of cycles, as visualized in Figure 9. The difference of stress amplitude at 100 cycles and 2000 cycles is about –10%. Therefore, in the current study, the cyclic behavior is solely described by the kinematic hardening during cyclic plasticity deformation and the isotropic softening is neglected in the flow rule. As a consequence, the stress–strain hysteresis obtained from the finite-element simulations does not show any dependence on the cycle number. Note that C and D batches (90° inclination of specimen/loading axis to building direction) exhibit higher stresses than A and B batches (0° inclination). This difference in the stress amplitude caused by the sample orientation with respect to the building direction is considerably larger than

Table 1. Elastic and constitutive material parameters for 316L steel at room temperature.

Parameter	Value
c_{11} [GPa]	256.5
c_{12} [GPa]	111.1
c_{44} [GPa]	72.7
$\dot{\gamma}_0$ [s ^{−1}]	0.001
Q [kJ mol ^{−1}] ^[22]	200
R [J mol ^{−1} K ^{−1}]	8.314
T [K]	294.15
$\tau_{c,0}^\alpha$ [MPa] ^[22]	170
p_1 [−] ^[22]	1250
A [MPa] ^[22]	5000
B [−] ^[22]	100
M [−] ^[22]	10

the difference caused by the larger layer thickness/grain size between the batches A and B and also for batches C and D.

The anisotropic elastic constants for the single-crystalline material within each grain were obtained based on the Young’s modulus estimated from the experimental tests and the proposed relation between anisotropic elastic constants and the Young’s modulus in ref. [30]. The plastic and kinematic hardening parameters defined in Equation (6) and (7) are calibrated in previous work^[22] by an inverse analysis using experimental data of sample A for two different strain amplitudes and in a wide temperature range between room temperature and 750 °C. Even if in the present work the constitutive model was applied only for room-temperature simulations for one strain amplitude, the parameters were not changed. All parameters in the flow rule are listed in Table 1.

4. Comparison between Numerical and Experimental Results

Figure 10 visualizes the cyclic deformation behavior of the prepared samples based on the experimental tests and the developed numerical model. As already seen in Figure 9, the differences in the mechanical behavior of the different batches are rather small, but the stress amplitudes reached for samples A and B, loaded in building direction, are somewhat lower than for samples C and D, loaded normal to the building direction. Figure 10a compares the cyclic response of samples A and B more closely and reveals that sample A with the smaller grain size reaches slightly higher stress levels during the strain-controlled cyclic loading. As shown in Figure 2 and 3, the crystallographic texture of samples A and B is comparable, with a slightly more pronounced <110> texture for sample A such that the higher stress amplitude for sample A is mostly attributed to the grain size effect.

The results of the micromechanical model show a generally good agreement with the experimental hysteresis curves with the largest discrepancies occurring in the transition regions between elastic and plastic material response. Here, the

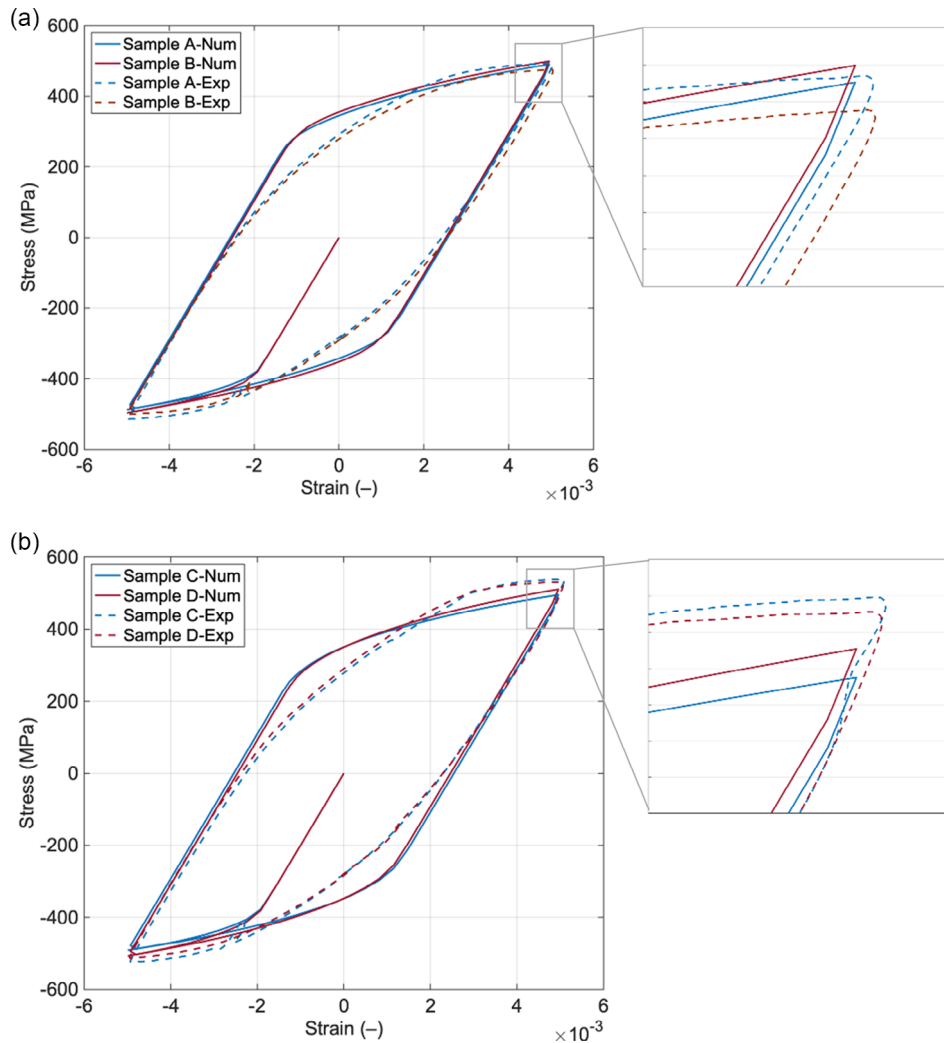


Figure 10. Comparison of stress–strain hysteresis loops between numerical results and experimental data for a) samples A and B and b) samples C and D.

experimental results indicate a significantly stronger Bauschinger effect and a reversal of the plastic deformation even slightly before the stress changes its sign during cycling, whereas the numerical results follow the elastic slope up to higher stresses before the transition to plastic yielding occurs. It is noted here again that the constitutive parameters for the crystal plasticity model were fit to match the cyclic plasticity of sample A in a wide temperature range and that the main focus of the fitting was to match the stress amplitudes for different applied strain cycles.^[22] Furthermore, in the present work, a local crystal plasticity model was applied in which length scales are not considered explicitly such that grain size effects are not captured by the model. Consequently, the numerical results reflect mostly the influence of crystallographic texture, grain morphology, and grain arrangement in the RVE. Since both factors are similar for samples A and B, the mechanical response in the model results is very similar as well. However, the stress amplitude of sample B is insignificantly higher, possibly due to the less pronounced texture in that sample, as will be discussed later.

Figure 10b compares the cyclic response of samples C and D based on the experimental tests. Again, it is seen that sample C with the smaller grain size reveals a slightly larger stress amplitude than sample D, although this effect is even less pronounced than that for the pair A/B. Similar to that pair, it is found again that the largest errors in the simulated stress–strain response occur in the transition between elastic and plastic material response. The stress amplitudes are predicted rather accurately by the model. Furthermore, when quantitatively comparing the behavior of the samples with the different orientations between building direction and loading axis, it is seen that the model correctly predicts that samples C and D are slightly stronger than samples A and B, reflected in somewhat lower stress amplitudes for the latter pair. The experimental results, furthermore, exhibit a slight difference in the work hardening behavior between pairs A/B and C/D, respectively, where the hardening behavior of the former pair is parabolic, whereas the latter pair shows initially a rather linear hardening behavior followed by an abrupt transition into an almost ideal plastic regime, where the stress remains rather constant.

5. The Origin of Plastic Anisotropy

As seen in the previous section, the material behavior between the differently oriented sample pairs A/B and C/D was slightly but significantly different. In this section, the origin of this plastic anisotropy in the additively manufactured samples is investigated. In general, anisotropy in the mechanical behavior of a material can be attributed to different factors, as crystallographic texture, grain aspect ratio, pore aspect ratio, etc. In Prasad et al.'s study,^[31] it has been shown that the anisotropy caused by elongated pores is rather insignificant for realistic porosities of an additively manufactured material. Only for pore volume fractions larger than 2% this would create a noticeable anisotropic material response. Hence, this influence is excluded here, and this work focusses solely on the influence of grain shape and texture on anisotropic mechanical behavior.

To accomplish this, the cyclic response of the RVE, mimicking the microstructure and crystallographic texture of sample A, was simulated along three loading directions (x -, y -, and z -axis). Referring to Figure 6 and 7, it is pointed out that the x -axis of the RVE reflects the building direction of the experimental

sample with respect to both the orientation of the elongated grains and the axis of crystallographic texture. The numerical results visualized in Figure 11a indicate that the building direction is the softest direction, where the difference in stress amplitude compared to the two other directions amounts to a value of about 3%. Hence, the plastic anisotropy is visible but not very pronounced.

To cross-validate this result, the cyclic stress–strain response of the same microstructure morphology of RVE-type A, that is, with the same grain geometries in the finite-element model, as in Figure 6a, was also investigated after assigning different crystallographic orientations to the grains, this time reflecting a random texture generated by the software toolbox MTEX.^[23] Figure 11b represents the results obtained for this RVE with a random texture loaded along different directions. It is evident that the mechanical response is rather isotropic, as all stress–strain curves are overlapping.

This result implies that the crystallographic texture has a much more significant influence on the macroscopic mechanical response of a material than the grain shape, at least for moderate aspect ratios of the elongated grains; similar to the results

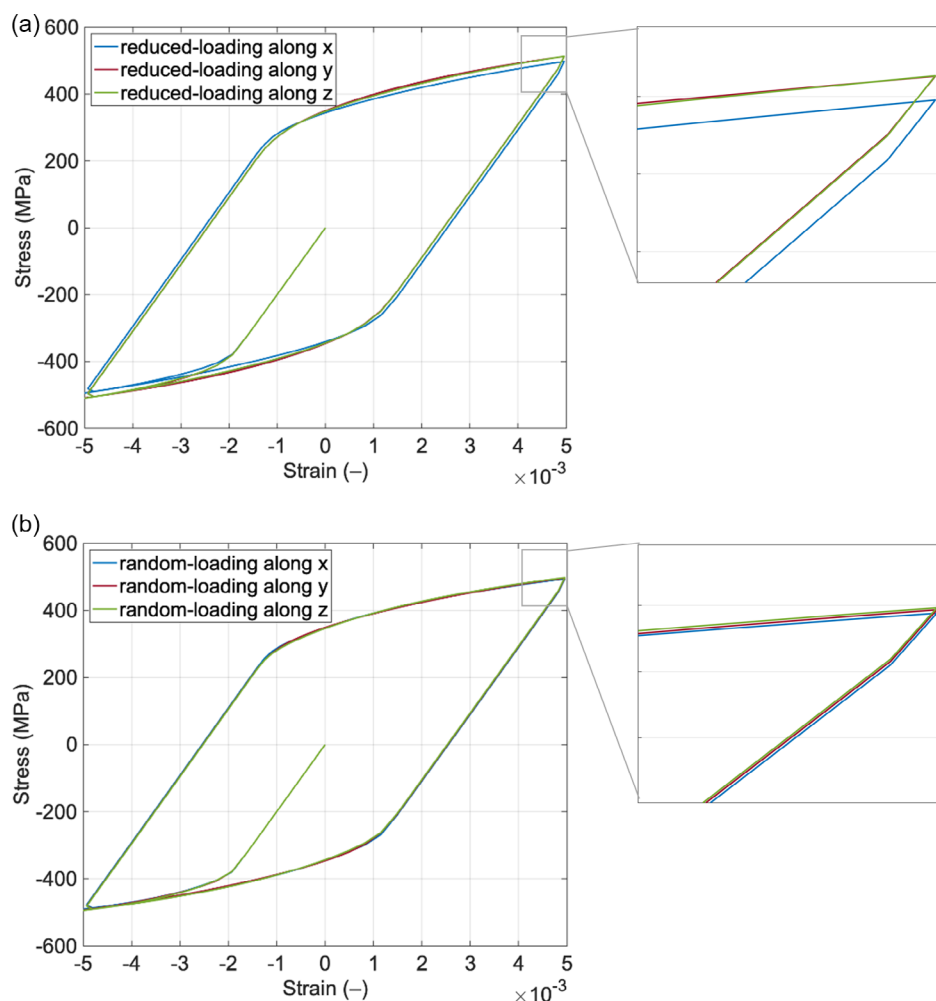


Figure 11. Stress–strain hysteresis loops for three orthogonal loading directions considering elongated grain shapes based on EBSD analysis of sample A, see Figure 6a, a) with a reduced texture, mimicking the real texture with 96 grain orientations, and b) a random texture.

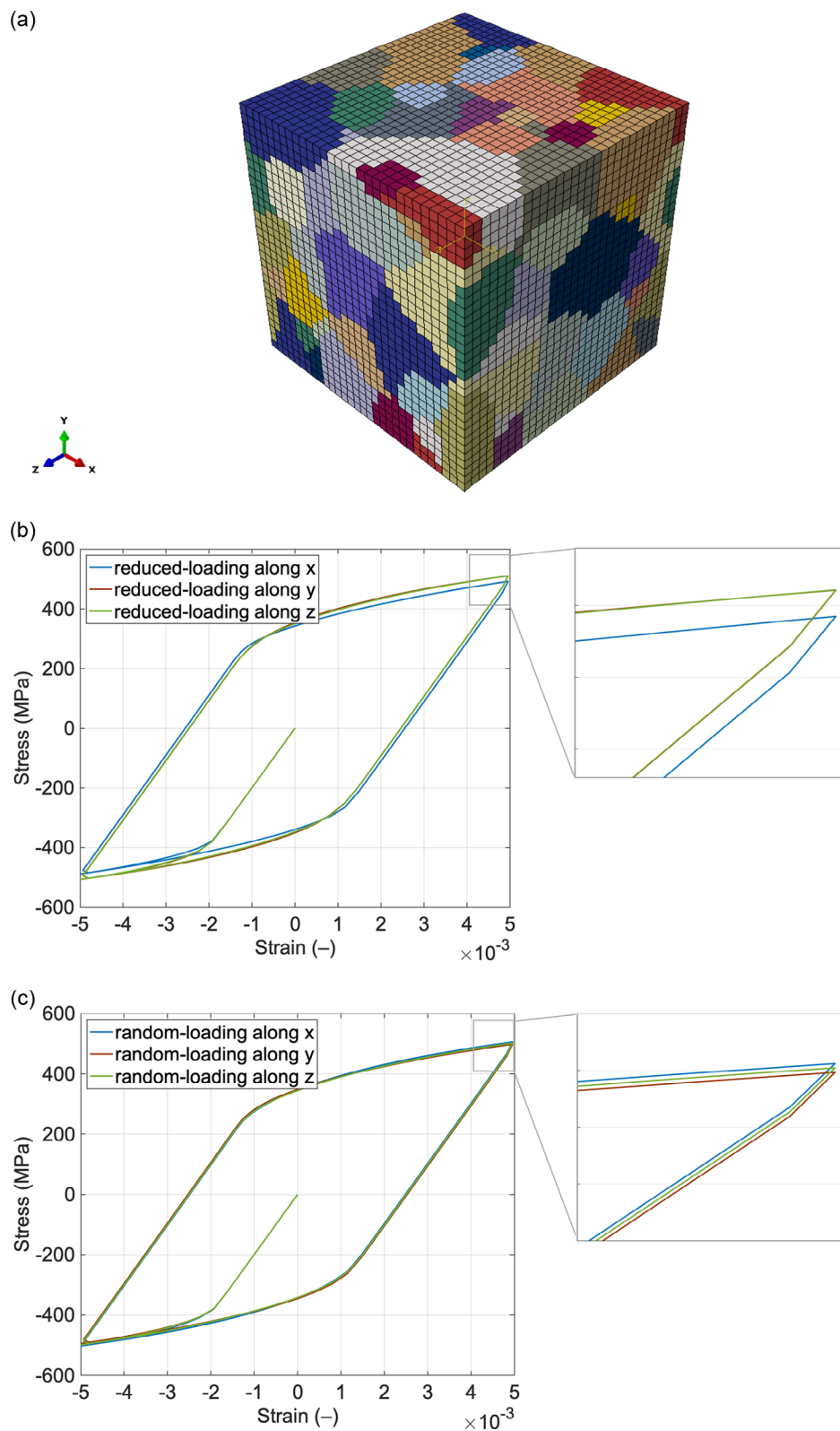


Figure 12. Stress–strain hysteresis loops for three orthogonal loading directions obtained from a) an RVE with equiaxed grains, b) with a reduced texture, mimicking the real texture with 96 grain orientations, and c) a random texture.

reported in ref. [27]. In experimental studies of cold-rolled sheet metal of 316L at room temperature, it was also reported that grains oriented in the crystallographic $\langle 110 \rangle$ direction behave in a softer way than grains in $\langle 111 \rangle$ or $\langle 100 \rangle$ orientation.^[32]

To further verify these findings, an RVE with 96 equiaxed, instead of elongated, grains was created, see Figure 12a, and simulated with same sets of crystallographic orientations for the grains as before, that is, mimicking the experimental texture and a random texture. It is seen in Figure 12b that for the realistic texture, described by the reduced set of 96 grain orientations, the same anisotropic behavior as for elongated grains is visible and still loading along the x -axis leads to the softest response

although the grain geometries do not single out any orientation in this case. The simulation results obtained for the random texture shown in Figure 12c, in contrast, reveal that all loading axes lead to a similar mechanical behavior, resulting in an isotropic response of the equiaxed microstructure, as observed before for the RVE with elongated grains in Figure 11b.

6. Analysis Stress and Strain within the Microstructure

The previous sections of this work only considered the macroscopic response of the different RVE to an applied cyclic load,

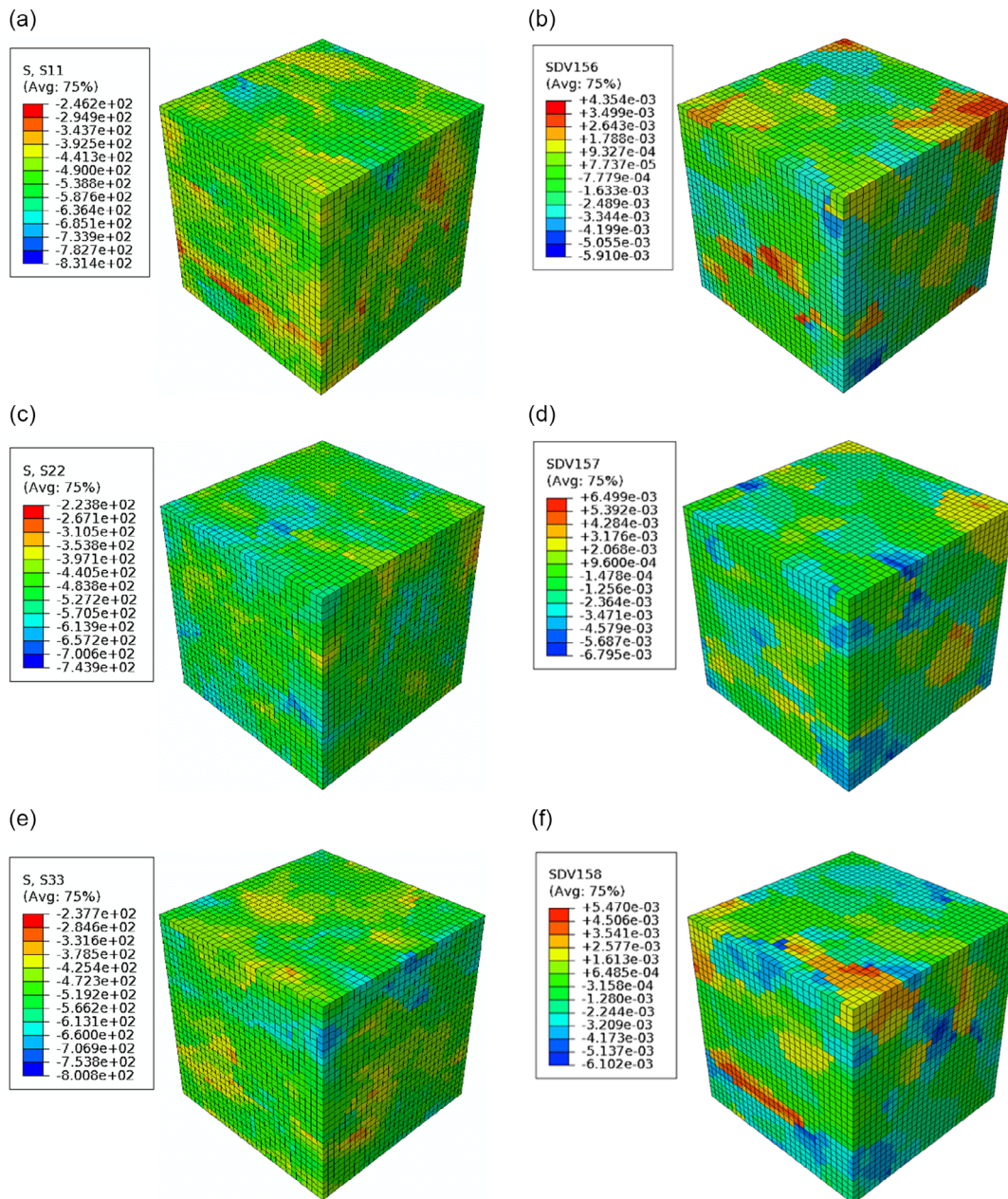


Figure 13. Distribution of local stresses (left) and plastic strains (right) for sample A after a full load cycle in a,b) x -direction along, c,d) y -direction, and e, f) z -direction. The stress and plastic strain components in the loading direction are plotted. The orientation of the models is the same as in Figure 6.

which can be directly compared to experimental results of uniaxial fatigue tests. However, one advantage of micromechanical modeling is that it can provide further insight into the local distribution of stress and strain within the microstructure. **Figure 13** shows the distribution of different components of the tensors of stress and plastic strain in the RVE generated according to the microstructure and crystallographic texture of experimental sample A, as shown in Figure 6a and 7. The results presented here correspond to the situation obtained under different loading directions when the maximum compressive strain after the first full load cycle is reached. In each case, the components of stress and plastic strain in the loading direction are plotted.

It is seen that the local stresses during loading along the x -axis (building direction), shown in Figure 13a, reach the highest values compared to the results of other loading directions, Figure 13c,e. This is remarkable since the average or macroscopic stress level is the lowest for this loading direction. The stress distribution for the other loading directions reveals a comparatively homogenous pattern. Concerning the distribution of plastic strains shown in Figure 13b,d,f, it is seen in all cases that in some regions of the microstructure tensile plastic strains prevail although the maximum of the compressive load cycle is reached. A comparison with the grain geometry shown in Figure 6a indicates that the plastic strains are rather homogeneous within the grains and that large jumps occur at the grain boundaries. It is noted here that the use of a strain-gradient crystal plasticity model would leverage such steep gradients of the plastic strain at grain boundaries.

To further analyze these findings, **Figure 14** depicts the distribution of local stress and plastic strain components at the centroid of all elements in the numerical model for loading along the x -axis, that is, corresponding to Figure 13a for stresses

and 13b for plastic strains, respectively. Consequently, this data corresponds to the situation obtained at the maximum compressive strain at the end of the simulation. The stress histogram presented in Figure 14a reveals a mean value of stress equal to -488 MPa, corresponding to the macroscopic stress level at this loading stage. It is seen that the local stress values can be described very well by a normal distribution with a standard deviation of 63 MPa. The histogram of local plastic strains in Figure 14b reveals a threefold characteristic: The highest frequency occurs for finite elements with very small plastic strains around zero. A rather broad and high peak is seen for plastic strains in the compressive region around -0.2% . Furthermore, as indicated already, a very significant number of finite elements shows a tensile plastic strain even at the global maximum of the compressive strain. This analysis of the local stresses and strains, thus, reveals that the influence of the microstructure on these distributions is much stronger than expected from only evaluating macroscopic properties. Furthermore, it is seen that the local values of stress and plastic strain can differ very significantly from the global values. Since fatigue crack initiation and the resulting lifetime depend strongly on local plastic deformation, classic fatigue models considering only global values may not be suitable to describe the lifetime of such additively manufactured material. Low-cycle-fatigue tests considering the respective lifetime behavior are necessary to clarify this.

7. Conclusion

The cyclic behavior of samples of the austenitic stainless steel 316L produced by PBF-L/M with different parameters was investigated at room temperature using a combination of

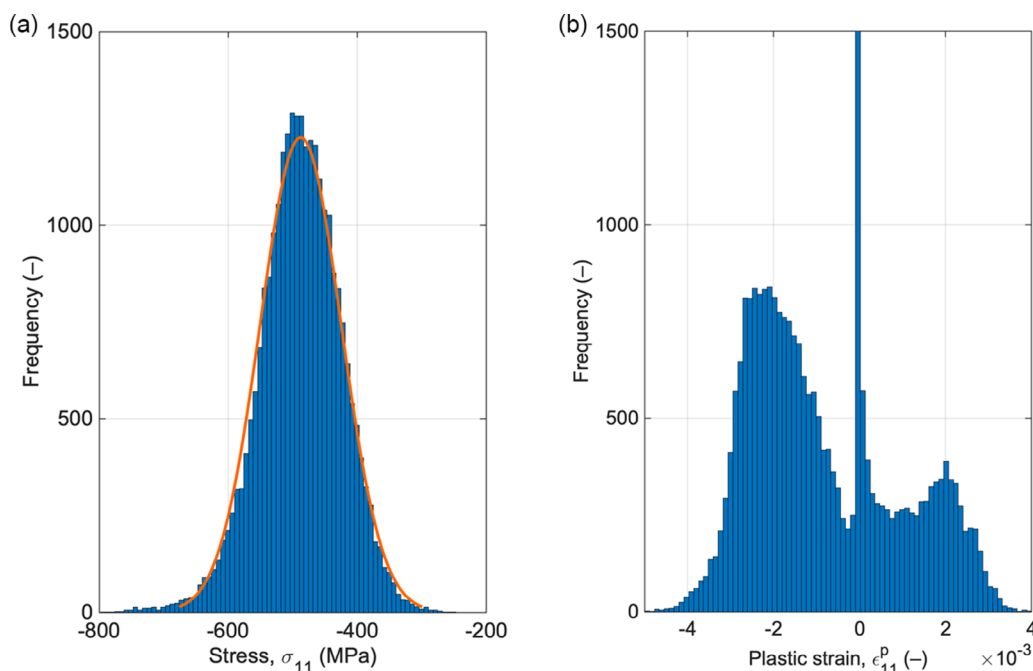


Figure 14. Distribution of a) stress and b) plastic strain values for each finite element in the simulation box at the maximum compressive strain at the end of the simulation. The red line in subfigure (a) represents a normal distribution with mean value of -488 MPa and a standard deviation of 63 MPa, which was fit to the histogram.

micromechanical modeling and experimental investigations. Two different specimen orientations of 0° and 90°, relating the specimen/loading axis to the building direction, were prepared and tested under symmetrical cyclic load. RVEs were generated for samples based on microstructural features as grain size, grain aspect ratio, tilt angle of the major axis, and the crystallographic orientations of the grains. The material behavior was described by anisotropic elastic constants for the elastic regime and crystal plasticity, taking into account kinematic hardening using the Ohno–Wang relation. The macroscopic material response obtained by finite-element simulations of the RVEs under cyclic loads can be directly compared to the experimental results, revealing a good agreement and a predictive capability of the micromechanical modeling approach.

The findings of this work clearly indicate that the crystallographic texture of the material is the key factor affecting its anisotropic mechanical behavior because samples tested along the building direction generally exhibit slightly lower stresses at the maxima of the displacement-controlled load cycles in comparison to specimens tested normal to their building direction. Microstructure analysis revealed a strong crystallographic texture with the crystallographic <110> axis along the building direction and a texture index of 2.7. The micromechanical modeling based on RVEs is in good agreement with the experimental results and clearly indicates that loading the material parallel to the <110> axis of the crystallographic texture results in a slightly softer response. Simulations with the same geometry of the elongated grains but considering a random texture, in contrast, resulted in quasiisotropic material behavior. Furthermore, the micromechanical simulations reveal that the influence of microstructure on local values of stress and plastic strain is significantly more pronounced than for the macroscopic values.

Supporting Information

Supporting Information is available from the Wiley Online Library or from the author.

Acknowledgements

The authors gratefully acknowledge funding of this project by the Deutsche Forschungsgemeinschaft (DFG, German Research Foundation), Project-ID 190389738, TRR 103. Furthermore, the authors thank Aleksander Kostka for support with the electron backscatter diffraction analysis.

Open Access funding enabled and organized by Projekt DEAL.

Conflict of Interest

The authors declare no conflict of interest.

Data Availability Statement

The data that support the findings of this study are available from the corresponding author upon reasonable request.

Keywords

additive manufacturing, anisotropic behaviors, crystal plasticity, crystallographic textures, micromechanical modeling

Received: January 23, 2023

Revised: April 26, 2023

Published online:

- [1] D. Herzog, V. Seyda, E. Wycisk, C. Emmelmann, *Acta Mater.* **2016**, 117, 371.
- [2] W. E. Frazier, *J. Mater. Eng. Perform.* **2014**, 23, 1917.
- [3] T. Niendorf, S. Leuders, A. Riemer, H. A. Richard, T. Tröster, D. Schwarze, *Metall. Mater. Trans. B* **2013**, 44, 794.
- [4] M. Shahmardani, A. Hartmaier, *Int. J. Fatigue* **2021**, 151, 106353.
- [5] R. Munier, C. Doudard, S. Calloch, B. Weber, *Proc. Eng.* **2010**, 2, 1741.
- [6] M. Poncelet, C. Doudard, S. Calloch, B. Weber, F. Hild, *J. Mech. Phys. Solids* **2010**, 58, 578.
- [7] N. Vajragupta, A. Ahmed, M. Boeff, A. Ma, A. Hartmaier, *Phys. Mesomech.* **2017**, 20, 343.
- [8] M. Shahmardani, N. Vajragupta, A. Hartmaier, *Crystals* **2021**, 11, 1473.
- [9] C. Mareau, V. Favier, B. Weber, A. Galtier, *Int. J. Fatigue* **2009**, 31, 1407.
- [10] C. Hennessey, G. M. Castelluccio, D. L. McDowell, *Mater. Sci. Eng., A* **2017**, 687, 241.
- [11] B. J. Schäfer, X. Song, P. Sonnweber-Ribic, H. ul Hassan, A. Hartmaier, *Metals* **2019**, 9, 368.
- [12] A. Paquin, S. Berbenni, V. Favier, X. Lemoine, M. Berveiller, *Int. J. Plast.* **2001**, 17, 1267.
- [13] S. Berbenni, V. Favier, M. Berveiller, *Int. J. Plast.* **2007**, 23, 114.
- [14] C. Mareau, V. Favier, B. Weber, A. Galtier, M. Berveiller, *Int. J. Plast.* **2012**, 32–33, 106.
- [15] A. Burgold, M. Droste, A. Seupel, M. Budnitzki, H. Biermann, M. Kuna, *Int. J. Plast.* **2020**, 133, 102792.
- [16] G. Moeini, A. Ramazani, S. Myslicki, V. Sundararaghavan, C. Könke, *Metals* **2017**, 7, 265.
- [17] F. Ogawa, T. Itoh, T. Yamamoto, *Int. J. Fatigue* **2018**, 110, 215.
- [18] T. Itoh, M. Sakane, K. Ohsuga, *Int. J. Press. Vessels Pip.* **2013**, 110, 50.
- [19] T. Itoh, H. Nakamura, M. Takanashi, M. Wu, *Theor. Appl. Fract. Mech.* **2017**, 90, 165.
- [20] A. Abdul-Latif, K. Saanouni, *Int. J. Plast.* **1996**, 12, 1123.
- [21] R. Xing, D. Yu, S. Shi, X. Chen, *Int. J. Plast.* **2019**, 120, 127.
- [22] M. Shahmardani, A. Hartmaier, *Metall. Mater. Trans. A* **2023**, 54, 1862.
- [23] F. Bachmann, R. Hielscher, H. Schaeben, *Solid State Phenom.* **2010**, 160, 1662.
- [24] <https://github.com/ICAMS/Kanapy.git> (accessed: June 2023).
- [25] M. R. G. Prasad, N. Vajragupta, A. Hartmaier, *J. Open Source Software* **2019**, 4, 1732.
- [26] A. Biswas, N. Vajragupta, R. Hielscher, A. Hartmaier, *J. Appl. Crystallogr.* **2020**, 53, 178.
- [27] A. Biswas, M. R. G. Prasad, N. Vajragupta, H. ul Hassan, F. Brenne, T. Niendorf, A. Hartmaier, *Adv. Eng. Mater.* **2019**, 21, 1900275.
- [28] ABAQUS/Standard, *Theory and User's Manuals*, HKS Inc., Pawtucket, RI **2016**.
- [29] N. Ohno, J. D. Wang, *Int. J. Plast.* **1993**, 9, 375.
- [30] R. F. S. Hearmon, *Rev. Mod. Phys.* **1946**, 18, 409.
- [31] M. R. G. Prasad, A. Biswas, K. Geenen, W. Amin, S. Gao, J. Lian, A. Röttger, N. Vajragupta, A. Hartmaier, *Adv. Eng. Mater.* **2020**, 22, 2000641.
- [32] M. Mineur, P. Villechaise, J. Mendez, *Mater. Sci. Eng., A* **2000**, 286, 257.